Verifying Larché–Cahn elasticity, a milestone of 20th-century thermodynamics

Shan Shi[a,b], Jürgen Markmann[a,b], and Jörg Weissmüller[a,b,1]

[a]Institute of Materials Research, Materials Mechanics, Helmholtz-Zentrum Geesthacht, 21502 Geesthacht, Germany; and [b]Institute of Materials Physics and Technology, Hamburg University of Technology, 21073 Hamburg, Germany

Edited by David Embury, McMaster University, Hamilton, Ontario, Canada, and accepted by Editorial Board Member Zachary Fisk September 6, 2018 (received for review May 31, 2018)

Many materials phenomena are governed by the interaction between chemistry and mechanics. However, it was only in the second half of the 20th century that the theory of open system elasticity by Francis Larché and John W. Cahn concatenated the fields of solid mechanics and alloy chemistry. As the theory's central materials descriptors, the open system elastic parameters describe how solids deform under stress when solute can rearrange at equilibrium while the chemical potential is held constant. Here, we report experiments verifying the predictions for these parameters. We study the elasticity of nanoporous Pd-H and Pd-Au-H during load cycles imposed by a dynamic mechanical analyzer. Short diffusion paths afford fast equilibration of H in the local strain gradients that carry the macroscopic elastic deformation. The experiment is in excellent agreement with the theory, confirming a central prediction of one of the key contributions to 20th-century thermodynamics.

mechanochemical coupling | elasticity | solid mechanics | alloy thermodynamics | nanomaterials

Phenomena that depend critically on the interaction between chemistry and mechanics are ubiquitous in materials science. The interplay between stress and lithium diffusion in battery electrodes is a modern example, while the martensite transformation—which relies on the elastic distortion of a crystal lattice to enhance its solubility for interstitials—has been exploited for millennia in hardening steel. Additional examples are superalloys, where the interplay of chemical diffusion and elastic interaction creates and stabilizes the precipitate structure that gives turbine blades their high-temperature creep resistance, coherency effects that suppress the spontaneous decomposition of supersaturated solid solutions by spinodal decomposition, and Cottrell atmospheres around lattice dislocation cores that contribute to solid solution hardening in many engineering materials. Last but not least, damping phenomena in metals can arise from solute redistribution in response to cyclic variation of the anisotropy (Snoek effect) or the gradients (Gorsky effect) of stress fields.

By the mid-20th century, many mechanochemical coupling phenomena were supported by detailed theory. However, the descriptive approaches tended to be ad hoc and tailored to the specific problem, and it was only with the theory of open system elasticity by Francis Larché and John W. Cahn that a unifying approach became available (1, 2). The conditions for chemical equilibrium between homogeneous phases at hydrostatic pressure could be considered established since the work of J. W. Gibbs, and the mechanics of nonuniformly and nonhydrostatically stressed elastic solids (at constant composition) had been described even earlier. The Larché–Cahn theory goes beyond these insights in combining the conditions of chemical and mechanical equilibrium in a unified framework that allows for general nonuniform and nonhydrostatic stress states while admitting the full complexity of equations of state for the chemical potential in solid solutions. One of its central conclusions is that small strain scenarios of coupled chemoelastic equilibrium can be mapped onto classic problems of solid mechanics alone when the conventional fixed composition elastic constants of Hooke's law are replaced with new open system elastic parameters that are informed by the interaction of composition with stress at equilibrium.

By concatenating the fields of alloy thermochemistry and solid mechanics, the Larché–Cahn theory is one of the key advances in thermodynamics of the 20th century. The approach is embraced by many modern studies of phase transformations by theory and numerical modeling (3–9), and its predictions for the impact of stress on the chemical potential and, thereby, on the driving force for diffusion during lithium insertion are a current topic in the active field of battery research (10–12). The Larché–Cahn theory is also at the heart of an ongoing controversy about the extent of solute enrichment in Cottrell atmospheres and its consequences for stress shielding in dislocation plasticity (13–18). It is, therefore, surprising that central predictions of the theory have not seen direct verification by experiment. The closest were experiments on the elastic aftereffect in metal hydrides around 1970 (19, 20). That effect was first analyzed in pioneering theory by Vadim Gorsky, who predicted an elastic relaxation as solute is redistributed in stress gradients in a solid solution (21, 22). Gorsky effect measurements are now an established tool for determining diffusion constants from the time dependence of that relaxation (23). However, the open system elastic constants, which are the key materials' parameters of the Larché–Cahn theory, have not been measured and compared with the predictions.

Significance

By concatenating the fields of continuum mechanics and alloy thermodynamics in a unified framework, the theory of open system elasticity by Francis Larché and John W. Cahn achieved one of the key advances in thermodynamics of the 20th century. The theory's implications for the coupling between stress and composition are generally well acknowledged, yet selected issues are under debate. It is, therefore, dissatisfactory that the predictions for the open system elastic parameters—as the theory's central materials descriptors—await experimental verification. Here, we report that the variation of the open system Young's modulus of palladium hydride with composition is in excellent agreement with the prediction. This confirms a cornerstone of materials' theory.

Author contributions: S.S. and J.W. designed research; S.S. performed research; S.S. and J.W. analyzed data; and S.S., J.M., and J.W. wrote the paper.

The authors declare no conflict of interest.

This article is a PNAS Direct Submission. D.E. is a guest editor invited by the Editorial Board.

[1]To whom correspondence should be addressed. Email: weissmueller@tuhh.de.

This article contains supporting information online at www.pnas.org/lookup/suppl/doi:10.1073/pnas.1809355115/-/DCSupplemental.

Published online October 5, 2018.

Here, we exploit the fast equilibration of hydrogen in nanostructured Pd and Pd-based alloys (24–29) for quantitatively comparing closed and open system elastic responses in the same material. We show excellent agreement with the predictions by Larché and Cahn.

Open System Elasticity

Theory. Larché and Cahn (1, 2) consider a stressed network solid with mobile solute. With attention to interstitial solutions, they show that the solute chemical potential, μ, at equilibrium is uniform and that the stress–strain relation can be derived from open system elastic parameters, such as the compliance $S^{\mu}_{ijkl} = \mathrm{d}E_{ij}/\mathrm{d}\,T_{kl}|_{\mu}$, where $\mathbf{T}$ and $\mathbf{E}$ denote the stress and strain tensors, respectively. For isotropic solids, the open system shear and Young's moduli are (1) $G^{\mu} = G^{x}$ and

$$Y^{\mu} = \frac{Y^{\mathrm{x}}}{1 + \chi\eta^2\, Y^{\mathrm{x}}}, \qquad [1]$$

respectively, where G^{x} and Y^{x} are the corresponding elastic constants at constant composition and χ is a solute susceptibility parameter, namely

$$\chi = \frac{1}{\rho_0}\frac{\mathrm{d}x}{\mathrm{d}\mu}\bigg|_{\mathbf{T}}, \qquad [2]$$

with x indicating the solute fraction and ρ_0 indicating the volumetric density of sites for solute. The concentration–strain coefficient η for isotropic solids is defined so that, at constant stress, the change δx in solute fraction induces the strain $\delta\mathbf{E} = \eta\mathbf{U}\delta x$, with $\mathbf{U}$ indicating the unit tensor in 3D.

It is well known that, owing to changes in the chemical bonding on alloying, the constant composition elastic parameters may explicitly depend on the composition [that is, $Y^{\mathrm{x}} = Y^{\mathrm{x}}(x)$]. However, Eq. **1** embodies an additional effect: Stress changes the composition at equilibrium, and along with that composition change comes an extra strain, which is over and above the classic elastic response and can be large. This implies a softening of the stress–strain relation. The solute atmosphere around the core of a lattice dislocation is an example: The stress field of the dislocation changes the composition, yet the composition change feeds back into the stress and reduces it. The open system elastic constants afford self-consistent solutions for the acting stress, which may then be used to evaluate the composition (17).

Fig. 1 illustrates the open system elastic behavior for the example of a regular interstitial solution. Taking the equation of state for the chemical potential as (30) $\mu = RT_{\mathrm{C}}((2-4x) + \tau\ln(x/(1-x)))$ (Fig. 1*A*), with T_{C} indicating the critical temperature of the miscibility gap, R indicating the molar gas constant, with $\tau = T/T_{\mathrm{C}}$, and using materials parameters (Y, η, T_{C}) (28) for Pd-H for the sake of illustration, the normalized open system elastic parameters are obtained as shown in Fig. 1*B* for temperatures below, at, and above T_{C}. It is seen that alloying drastically reduces Young's modulus at any temperature. Y^{μ} can even drop all of the way to zero, notably at the critical point and at the spinodals. A finite strain can then result from an infinitely small stress.

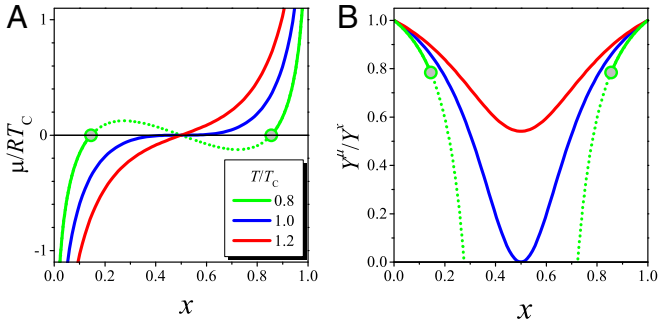

Fig. 1. Open system elasticity in a regular solution. (*A*) Chemical potential, μ, vs. solute fraction, x, for temperatures T below, at, and above the critical temperature T_{C}. (*B*) Open system Young's modulus, Y^{μ}, normalized to the closed system Young's modulus, Y^{x}, vs. x. Note the drastic reduction in Y^{μ} depending on T and x. Dashed lines indicate metastable or unstable states in the miscibility gap. The system is elastically instable ($Y^{\mu} < 0$) between the spinodals.

For use below, we introduce the uniaxial compliance as $S_{\mathrm{U}} = 1/Y$, and we note that Eq. **1** implies that the relative difference, Δs^{μ}, between the open system and closed system compliances, $\Delta s^{\mu} = S^{\mu}_{\mathrm{U}}/S^{x}_{\mathrm{U}} - 1$, obeys

$$\Delta s^{\mu} = \chi\eta^2\, Y^{x}. \qquad [3]$$

Verification Strategy. Our verification strategy exploits the fast diffusion of hydrogen in Pd and its alloys. The chemical potential, μ_{H}, of H may conveniently and precisely be controlled by the electrode potential, E, of the metal immersed in acids. The wide miscibility gap of Pd-H at room temperature (31) implies that Pd-H alloys with intermediate hydrogen fraction cannot be obtained as homogeneous, single-phase states. Yet, alloying coinage metals atom fractions in the order of few 10% reduces T_{C} of the gap to room temperature (31–35). There is then a wide range of solubility for H.

We choose dynamic mechanical analysis (DMA) for exploring elasticity as the function of μ_{H}. Uniform tension or compression loading is not convenient, as a variation in the equilibrium value of the net H content in a sample would be entailed. This would require H uptake or release through the sample surface, a process that involves kinetic barriers and, therefore, can be slow (36). Instead, we explore the geometry considered by Gorsky (22), where the solute redistributes internally in strain gradients when a beam is bent. The net hydrogen fraction may then be approximated as constant within a linear theory that applies at small strain, and the kinetics is entirely controlled by the bulk diffusion constant.

Conventional DMA frequencies are in the order of 1–100 Hz so that the characteristic time t for H equilibration should not exceed $t = 1$ ms. With the H diffusion constant, D, in the bulk of Pd at 300 K in the order of $4\times10^{-11}\ \mathrm{m}^2/\mathrm{s}$ (37) and with the characteristic diffusion distance $X \sim \sqrt{(Dt)}$, we must require that the beam thickness is below 200 nm.

Dealloying, the selective dissolution of a less noble component from a solid solution by corrosion (38, 39), affords the preparation of nanoporous (np) metal samples with macroscale dimensions, suitable for investigation by DMA (40). Their microstructure takes the form of a network of struts or "ligaments" with sizes in the order of a few tens of nanometers or below. The effective macroscopic elastic response of these materials to uniaxial compressive external load is carried, at the ligament level, by predominantly bending, while an additional small axial component may be admitted (41). Bending deformation sets up stress gradients along cross-sections of a ligament (that is, on the characteristic scale of the ligament size). Axial deformation is nonuniform on a slightly larger scale, with neighboring ligaments tending to be strained more in compression or more in tension, depending on their orientation to the load axis (42). In any case, external load on dealloyed np metals sets up local stress gradients that may drive solute redistribution as in a Gorsky-type scenario.

The stiffness of struts against both deformation modes, axial strain and bending, is governed by Young's modulus as the relevant elastic parameter. This implies that relative changes—such as those of Eq. **1**—in the local Young's modulus, Y,

of the material in the struts translate one to one into relative changes of the effective macroscopic Young's modulus, Y^{eff}. In other words,

$$\Delta Y^{\mathrm{eff}} / Y^{\mathrm{eff}} = \Delta Y / Y. \quad [4]$$

Uniform samples of dealloying-made np Pd have recently become available and exhibit H sorption characteristics quantitatively compatible with conventional massive Pd (29). Thus, DMA experiments with electrochemical control of the H fraction in np Pd or Pd-Au are consistent with our strategy.

Results

Microstructure and Hydrogen Sorption. We study two types of monolithic, millimeter-sized np samples (details are in *SI Appendix*). For one type, np Pd is prepared by dealloying $Cu_{85}Pd_{15}$ as in ref. 29. That material contains 5 atomic percent (at. %) of residual Cu and has a solid volume fraction of 0.17. For the other type, samples of np Pd-Au, nominally np $Pd_{83}Au_{17}$, are made by dealloying $Cu_{85}Pd_{12.5}Au_{2.5}$. Accounting for the residual Cu, the np Pd-Au samples' composition is $Pd_{77}Au_{15.5}Cu_{7.5}$. Metal fractions after dealloying could be determined with an uncertainty of ± 1 at.-%.

Scanning electron micrographs of cleavage surfaces are shown in Fig. 2 *A* and *B*. As reported in ref. 29, np Pd has a hierarchical structure, with the mean ligament size, L, at the lower hierarchy level below 10 nm. By contrast, np Pd-Au exhibits a unimodal structure with $L = 7$ nm. Fig. 2 *A*, *Inset* and *B*, *Inset* shows overviews of the cleavage surface of np Pd and of the outer surface of np Pd-Au. The uniform microstructure is apparent, as is the absence of macroscopic cracks.

The chemical potential μ_{H} of hydrogen in the np samples was established by immersion in sulfuric acid and control of the electrode potential E_{SHE} [measured relative to the standard hydrogen electrode (SHE)], $\mu_{\mathrm{H}} = -FE_{\mathrm{SHE}}$, with F indicating Faraday's constant. Unless otherwise stated, the net hydrogen atom fraction, $x_{\mathrm{H}}^{\mathrm{net}}$ (H per metal atom), was determined from the relative change, $\Delta l/l$, in sample dimension, l, exploiting the linear relation between l and $x_{\mathrm{H}}^{\mathrm{net}}$ (43, 44) and the previously established concentration–strain coefficient of our material (29) (*SI Appendix* has details).

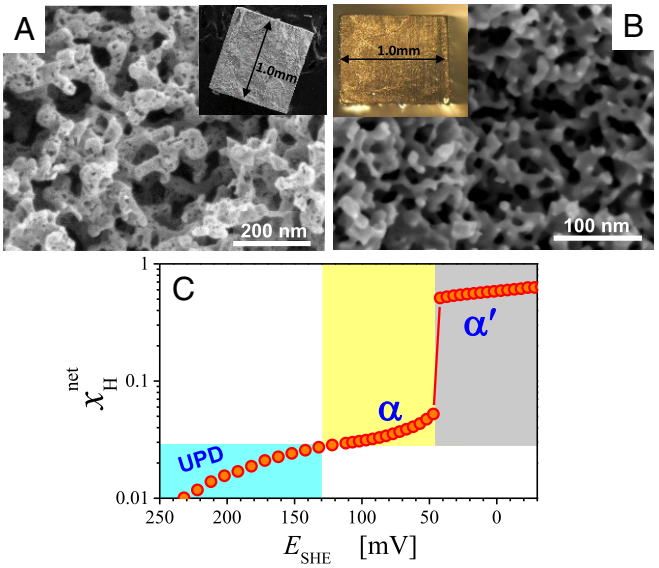

Fig. 2. Microstructure and H sorption. (*A*) Scanning electron micrograph of np Pd; *Inset* shows cross-sectional (cleavage) surface. (*B*) Scanning electron micrograph of np Pd-Au; *Inset* shows optical micrograph of outer surface. (*C*) Net (including surface adsorption plus bulk absorption) hydrogen fraction ($x_{\mathrm{H}}^{\mathrm{net}}$) vs. electrode potential (E_{SHE}) for np Pd. Regimes of H UPD on the pore surfaces and of bulk hydrogen sorption in the dilute α and the concentrated α' phase are marked. Data are from ref. 29; x_{H} is measured by current integration.

For the example of np Pd, Fig. 2*C* shows adsorption isotherms of $x_{\mathrm{H}}^{\mathrm{net}}$ vs. E_{SHE}, here determined by current integration (*SI Appendix*). The graph resolves three regimes: H adsorption [or underpotential deposition (UPD)] on the surface followed by H absorption in the bulk of, first, the dilute α-Pd-H and then, the concentrated α'-Pd-H phase (29). We found that np Pd can be cycled through the $\alpha - \alpha'$ phase transformation and back for $\gg 1{,}000$ cycles without substantial change in the microstructure or the sorption behavior (29).

As the reference state for zero hydrogen fraction, we chose the equilibrated sample at the potential of the onset of bulk absorption. This is at $E = 0.130 \pm 0.005$ V for the np Pd-H sample in Fig. 2*C*. Thus, our reference state is the sample with sensibly no hydrogen in the bulk and with an essentially saturated UPD adsorption layer at the surface. For conciseness of notation, we henceforth refer to the bulk hydrogen fraction (excluding the UPD H) per total number of metal atoms as x_{H}. In some instances, we normalize the effective Young's modulus to its "reference" value, Y_0^{eff}; that value refers also to the above reference state.

Isotherms of x_{H} vs. E were obtained by slow-scan cyclic voltammetry. Fig. 3*A* shows E vs. x_{H} in np Pd at different potential scan rates. Also shown is an isotherm from ref. 29 based on an even slower approach with equilibration at discrete potential values. The phase transition plateau and hysteresis are obvious in all graphs. As the scan rate decreases, the hysteresis lessens, and the graphs for intermediate hydrogen fraction approach horizontal lines. This is consistent with the well-known miscibility gap in the alloy. Fig. 3*B* displays the isotherms for np Pd-Au. Again, the hysteresis systematically lessens at smaller scan rate. However, the graphs remain sloped at all scan rates. This suggests a very small miscibility gap or even continuous solubility for H. The data, and specifically the nearly continuous solubility of H, are consistent with data for $Pd_{85}Au_{15}$ in ref. 35.

Fig. 3 *C* and *D* refers to the evaluation of the solute susceptibility, χ. The evaluation has been restricted to solutions that are homogeneous and dilute in H (see also the discussion of solubility limit below) measured during increasing x_{H} and at the lowest scan rate. That scenario avoids large current densities as well as hysteresis, thereby providing the most reliable data. Fig. 3*C* plots the solubility isotherms in that regime vs. μ_{H}. The general magnitude and the downward curvature at higher x_{H} are consistent with the literature. A slight upward curvature at the very lowest x_{H} is not compatible with dilute solution behavior in the bulk and may be explained as the result of some extra hydrogen being absorbed during the approach to saturation in the UPD layers. For each material, the isotherm was approximated as a polynomial in $\ln(x_{\mathrm{H}})$ (dashed lines in Fig. 3*C*), and χ was obtained by taking the derivative algebraically according to Eq. **2**. The results are shown in Fig. 3*D*. It is seen that np Pd-Au, due to its higher solubility, reaches a larger susceptibility value. It is expected that χ converges to zero in the limit of high dilution. The observation of a finite χ at the lowest x_{H} is, therefore, again a signature of a small extra H uptake while the UPD layers approach saturation. In other words, our data slightly overestimate χ at the lowest x_{H}.

DMA. Details of our DMA experiments are shown in *SI Appendix*. *SI Appendix*, Fig. S1*A* shows the setup with an electrochemical cell, affording control of μ_{H} during simultaneous measurements of the (effective, macroscopic) Young's storage modulus Y^{eff}, the loss modulus $Y_{\mathrm{loss}}^{\mathrm{eff}}$, and the sample length

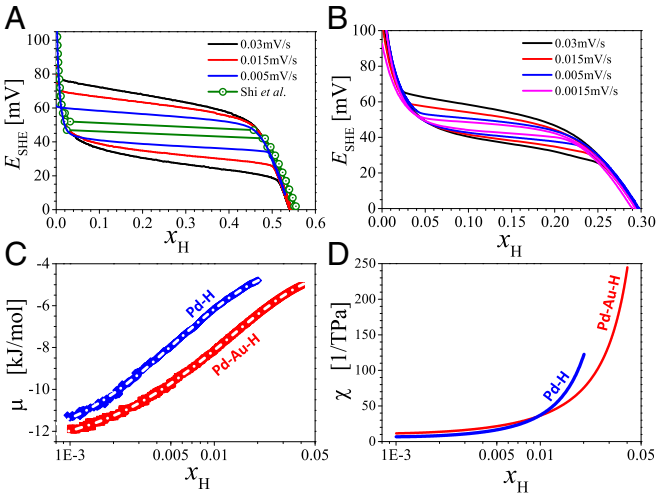

Fig. 3. Hydrogen solubility isotherms and solute susceptibility. Electrode potential, E_{SHE}, vs. bulk hydrogen fraction, x_H, measured by in situ dilatometry from the length change during cyclic voltammetry. Different scan rates as indicated. (*A*) np Pd and (*B*) np Pd-Au. (*C*) Details for solutions that are dilute in H plotted as hydrogen chemical potential μ_H vs. x_H. Colored symbols (overlapping), experiment; white dashed lines, fits. (*D*) Solute susceptibility parameter χ vs. x_H. Included in *A* is an isotherm determined by current integration after potential jumps (even slower charging) in our earlier work (29).

change Δl, which implies the x_H. Measurements of Y^{eff} for np metals by DMA have been validated by comparison with conventional compression tests on np metal samples (40, 45). DMA signals for a representative potential scan through the $\alpha - \alpha'$ phase transition are shown in *SI Appendix*, Fig. S1*B*. The elastic response was reproducible and stable over time (*SI Appendix*, Fig. S2). Experiments with np Pd-H in single-phase regimes and at strain frequencies, ν, in the range from 0.1 to 100 Hz (*SI Appendix*, Fig. S3*A*) found Y^{eff} to be independent of ν within better than 1.4%, irrespective of x_H. These results suggest that the elastic behavior under the conditions of our measurement is stable, reproducible, and independent of hydrogen diffusion kinetics.

Open System Elastic Response. The symbols and left ordinates in Fig. 4 *A* and *B* explore how Y^{eff} for np Pd and np Pd-Au varies with x_H at strain frequency of 1 Hz. To emphasize the relative change on hydriding, Y^{eff} is normalized to the value, Y_0^{eff}, in the reference state. As the most obvious observation, the stiffness—which is at maximum for the pure (hydrogen-free) metals—goes through a pronounced dip as x_H increases. Near the largest x_H, the values of Y^{eff} still remain below those in the pure metals. Most importantly, the decrease in Y^{eff} starts immediately on hydriding and Y^{eff} is substantially reduced already before the onset of the phase transformation.

The excellent consistency of the Y^{eff} data for scan rates 0.2, 0.1, and 0.03 mV/s suggests that the equilibration is sufficient for a meaningful measurement of the elastic response in the hydrided states. A pronounced hysteresis between adsorption and desorption is apparent for np Pd. By contrast, the adsorption and desorption branches coincide for np Pd-Au. This behavior is consistent with the hysteresis that is generally observed when cycling Pd-H through the $\alpha - \alpha'$ miscibility gap and with the expectation that the gap is suppressed in Pd-Au-H.

To emphasize the gain in compliance due to hydrogen absorption, we have also converted the stiffness data of Fig. 4 *A* and *B* into relative compliance changes, Δs^{eff}. The lines and right ordinates in Fig. 4 *A* and *B* show this data. Remarkably, H electrosorption can result in as much as a 30% increase in compliance.

Fig. 4*C* shows that the loss factor, $\tan\delta = Y_{loss}^{eff}/Y^{eff}$, of np Pd-H increases steeply when entering a two-phase state; this steep increase qualifies $\tan\delta$ as a sensitive indicator of the onset of the phase transformation. In the two-phase states, $\tan\delta$ depends on the potential scan rate. The observations suggest that two-phase np samples exhibit microstructural heterogeneity on a scale that is (*i*) larger than the ligament size and (*ii*) dependent on the rate at which the phase transformation is driven. The larger scale would make for slower hydrogen equilibration during strain cycles. The observations for np Pd-Au-H (Fig. 4*D*) are quite similar, suggesting a region of two-phase coexistence or at least large compositional heterogeneity at intermediate values of x_H in the ternary alloy. Because of the incomplete equilibration, data from the two-phase states need to be excluded from our comparison with the theory for open system elasticity. Inspection of Fig. 4 *C* and *D*, therefore, suggests that this comparison, presented below, needs to be restricted to hydrogen fractions $x_H < 2\%$ for np Pd and $< 4\%$ for np Pd-Au.

Investigations on the frequency dependence of $\tan\delta$ are shown in *SI Appendix*, Fig. S3*B*. In single-phase states and at frequencies up to 10 Hz, the loss factor is found to be (*i*) very small, (*ii*) practically identical to that in "dry" np Pd samples measured in air, and (*iii*) independent of the strain frequency. These observations verify that the loss in single-phase states is not related to hydrogen, confirming that H here redistributes much faster than the characteristic time of a strain cycle.

The theory prediction for the relative change in open system compliance with x_H is obtained from Eq. **3** using the experimental value for η of our material from ref. 29 and the experimental data for χ from Fig. 3*D*. For Young's modulus of pure Pd, we chose the value of the polycrystalline metal, 120 GPa (46). Finite element method (FEM) simulations confirm that the polycrystalline Young's modulus correctly parameterizes the local elastic response of the ligaments in dealloyed np metal: FEM of the effective elastic behavior of realistic np microstructures achieves excellent agreement with experiments on np Au (47).

Consistent with Eq. **4**, the relative change in the effective macroscopic compliance is expected to agree with the relative

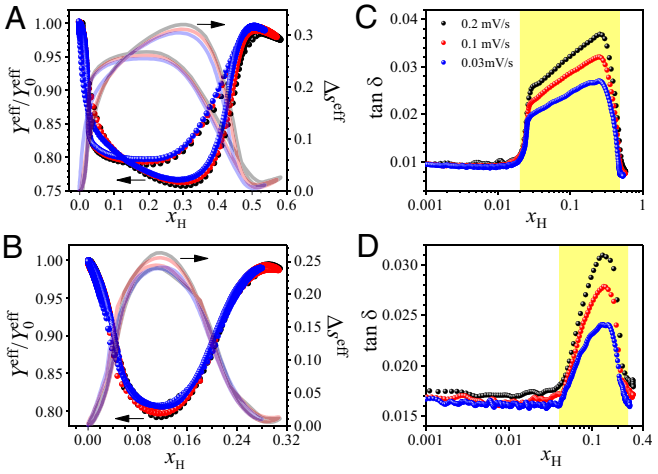

Fig. 4. Open system elastic response. In situ DMA on (*A* and *C*) np Pd and (*B* and *D*) np Pd-Au at different scan rates of the electrode potential as indicated. All data are for strain frequency 1 Hz and plotted vs. bulk hydrogen fraction, x_H. (*A* and *B*) Normalized Young's modulus, Y^{eff}/Y_0^{eff} (left ordinate and circles) and relative change, Δs^{eff}, in effective compliance (right ordinate and lines). (*C* and *D*) Loss factor, $\tan\delta$, during hydrogen absorption run. Shaded areas indicate two-phase states.

change of the local compliance. This motivates our comparison of theory and experiment for relative compliance change. Fig. 5 shows the theory as solid lines. Experimental data, measured at DMA frequencies of 1 and 3 Hz during hydrogen absorption runs with np Pd and np Pd-Au, are shown as circles in Fig. 5. At the lowest x_H, the theory slightly overestimates the compliance change. This is readily explained as a consequence of the slightly too large experimental χ values at the lowest x_H (see discussion above). As μ_H and x_H increase and as the experimental compliance change becomes significant, the graphs for theory and experiment converge and continue to vary with excellent agreement. Thus, the enhancement of the compliance in the single-phase dilute solutions is fully and quantitatively consistent with the theory of open system elasticity.

Discussion

Our central observation is the substantial increase in compliance when np Pd and Pd-Au are alloyed with hydrogen. The enhancement is largest—up to 30%—in two-phase states of the material, but substantial changes—up to 10%—are also found in single-phase states.

Previous studies of the elasticity of Pd-H used the ultrasound pulse-echo technique (48, 49) or resonances in millimeter-scale samples at ultrasonic frequencies (50, 51). It is readily confirmed that measurements of the elastic constants of single-phase samples of Pd-H with ultrasound probe the constant composition elastic behavior. At frequencies of several 100 kHz, each half cycle takes about 1 ms. The velocity of longitudinal sound waves in Pd is around 4 km/s (52), implying ultrasound wavelengths λ in the order 1 cm. The regions of compression and tension in the wave field here represent the heterogeneities in the stress between which solute has to be redistributed in an open system scenario. However, according to our estimates of the diffusion distance of H in Pd at room temperature (see above), the characteristic diffusion distance within 1 ms will be of order 10 nm. This is smaller than λ by six orders of magnitude. Obviously, hydrogen cannot follow the sound waves, and therefore, ultrasound experiments measure essentially the constant composition modulus.

The ultrasound data for single-phase states of Pd-H afford an estimate of the variation in constant composition elasticity. Focusing on dilute α-Pd-H, Salama and Ko (48) find the relative change in the polycrystalline (Voigt–Reuss average) Young's modulus at -0.5% per atomic percentage H, much smaller than the -6% change at 2 at.-% H in our study. Ultrasound data for the variation of Y with x_H in single-phase α'-Pd-H have not been reported, yet Schwarz and coworkers (51) studied the single-crystal shear elastic parameters C_{44} and $C' = (C_{11} - C_{12})/2$. Between pure Pd and the terminal α' solution, they report a decrease in C_{44} by several percent, while C' increases by a similar amount. Both parameters are then found to decrease on further hydrogen uptake. Our experiments on Y^{eff} also show a decrease between pure Pd and terminal α'-Pd-H yet with even less variation (1–2%).

The lack of data for the constant composition Young's modulus Y^x of α'-Pd-H prevents us from comparing experiment and theory in the more concentrated solutions. We thus focus on α-Pd-H, where all observations indicate that the small hydrogen fraction will not substantially affect the constant composition elastic response. These observations provide a priori justification for our use of the pure Pd Young's modulus for Y^x of α-Pd-H in Eqs. **1** and **3**. The excellent agreement between theory and experiment confirms this choice a posteriori: the pronounced increase in compliance of single-phase Pd-H with hydrogen content can be explained entirely as due to the transition from closed to open system elasticity.

Larger changes in the elastic constants, similar to these observations, have been reported for two-phase states of Pd-H (50, 51). In those studies, precipitates with characteristic size and spacing in the order of 1 μm (53) introduce elastic heterogeneity that interacts with the ultrasound wave field and leads to cyclic hydrogen redistribution on a scale much smaller than the wavelength (50). While the characteristic distance is still too large for complete equilibration of x_H within each half cycle of the ultrasound wave, the redistribution of H can here substantially enhance the compliance. In our experiments, the H redistribution in single-phase states is between the stretched and compressed regions of a ligament during bending deformation, which are a few nanometers apart. When the np samples enter a two-phase state, heterogeneity may arise on length scales much larger than the ligament diameter. The redistribution of hydrogen in the cyclic stress fields of our DMA experiment may then be qualitatively similar to that in the ultrasound experiments; this explains the large loss factor in two-phase states of our samples.

Our observation of a 30% change in the elastic behavior under control of the electrode potential is remarkable, since it implies a material with a compliance that can be adjusted on demand. Our experiments thus emphasize the potential of metal/electrolyte hybrid nanomaterials with operando tunable properties, which have been proposed in earlier work as novel functional materials (54, 55). The ability to manipulate a material's compliance in service may be relevant when the haptic behavior is to be adjusted or when mechanical or acoustic resonances are to be tuned.

Conclusion

Our work experimentally verifies the prediction of the theory of Larché and Cahn (1, 2) for the elastic parameters of open systems. Focusing on single phase, dilute alloys of hydrogen in Pd and Pd-Au, we examine how the stiffness varies with hydrogen content. We show that Young's modulus is substantially reduced when the alloy is hydrided, which is in quantitative agreement with the theory. It is well acknowledged that stress can change the composition of a solid solution at equilibrium. The elastic softening illustrates that, conversely, the composition change feeds back into the stress and can substantially reduce it. As one example for the implications, our observations would seem to support the controversial (13–18) suggestion that the stress fields around lattice dislocations in solid solutions will deviate noticeably from what is predicted by classic, constant composition elasticity theory.

Solute redistribution in stress gradients was first proposed by Vadim Gorsky (22), and the Gorsky effect was the subject of several profound experimental studies of the associated hydrogen diffusion phenomena in the second half of the 20th century. Larché and Cahn (1, 2) provide a thermomechanical framework that includes these effects but has a much more general scope.

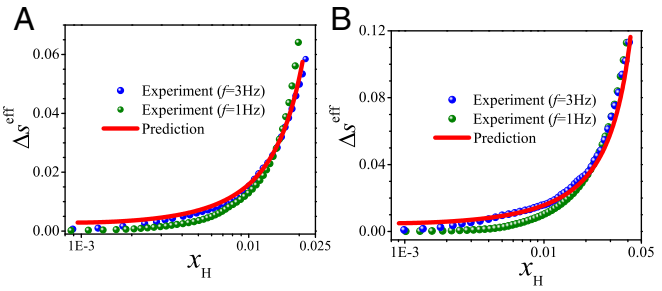

Fig. 5. Comparison of experiment and theory for relative compliance change. Relative compliance change, Δs^{eff}, vs. bulk hydrogen fraction, x_H, for (*A*) np Pd and (*B*) np Pd-Au. Experiments used cyclic voltammetry at a scan rate of 0.2 mV/s under DMA frequencies of 1 and 3 Hz. Theory prediction based on Eq. **3** used solute susceptibility data from Fig. 3*D*.

Our observations provide an essential experimental verification of this important contribution to 20th-century thermodynamics.

ACKNOWLEDGMENTS. S.S. acknowledges support from the China Scholarship Council.

1. Larché F, Cahn JW (1973) A linear theory of thermochemical equilibrium of solids under stress. *Acta Metall* 21:1051–1063.
2. Larché F, Cahn JW (1978) Non-linear theory of thermochemical equilibrium of solids under stress. *Acta Metall* 26:53–60.
3. Leo PH, Sekerka RF (1989) The effect of elastic fields on the morphological stability of a precipitate grown from solid-solution. *Acta Metall* 37:3139–3149.
4. Thompson ME, Su CS, Voorhees PW (1994) The equilibrium shape of a misfitting precipitate. *Acta Metall Mater* 42:2107–2122.
5. Fratzl P, Penrose O, Lebowitz JL (1999) Modeling of phase separation in alloys with coherent elastic misfit. *J Stat Phys* 95:1429–1503.
6. Mukherjee R, Abinandanan TA, Gururajan MP (2009) Phase field study of precipitate growth: Effect of misfit strain and interface curvature. *Acta Mater* 57:3947–3954.
7. McDowell MT, Lee SW, Nix WD, Cui Y (2013) 25th anniversary article: Understanding the lithiation of silicon and other alloying anodes for lithium-ion batteries. *Adv Mater* 25:4966–4984.
8. Chen L, et al. (2014) A phase-field model coupled with large elasto-plastic deformation: Application to lithiated silicon electrodes. *J Electrochem Soc* 161:F3164–F3172.
9. Mishin Y (2015) Calculation of open and closed system elastic coefficients for multicomponent solids. *Phys Rev B* 91:224107.
10. Cui Z, Gao F, Qu J (2012) A finite deformation stress-dependent chemical potential and its applications to lithium ion batteries. *J Mech Phys Sol* 60:1280–1295.
11. He YL, et al. (2014) Effects of concentration-dependent elastic modulus on the diffusion of lithium ions and diffusion induced stress in layered battery electrodes. *J Power Sourc* 248:517–523.
12. Mukhopadhyay A, Sheldon BW (2014) Deformation and stress in electrode materials for li-ion batteries. *Prog Mater Sci* 63:58–116.
13. Cahn JW (2013) Thermodynamic aspects of Cottrell atmospheres. *Phil Mag* 93:3741–3746.
14. Hirth JP (2014) On definitions and assumptions in the dislocation theory for solid solutions. *Phil Mag* 94:3162–3169.
15. Cahn JW (2014) Reprise: Partial chemical strain dislocations and their role in pinning dislocations to their atmospheres. *Phil Mag* 94:3170–3176.
16. Hirth JP (2014) Response to comments. *Phil Mag* 94:3177–3182.
17. Mishin Y, Cahn JW (2016) Thermodynamics of Cottrell atmospheres tested by atomistic simulations. *Acta Mater* 117:197–206.
18. Hirth JP, Barnett DM, Hoagland RG (2017) Solute atmospheres at dislocations. *Acta Mater* 131:574–593.
19. Alefeld G, Schaumann G, Tretkowski J, Völkl J (1969) Ferroelasticity of niobium due to hydrogen as a lattice gas. *Phys Rev Lett* 22:697–700.
20. Völkl J (1972) The Gorsky effect. *Berichte Bunsenges Phys Chem* 76:797–805.
21. Hardouin Duparc O, Krajnikov A (2017) Vadim Gorsky, a forgotten physics pioneer. *Physics Today*, 10.1063/PT.6.4.20170713a.
22. Gorsky WS (1935) Theorie der elastischen Nachwirkung in ungeordneten Mischkristallen (elastische Nachwirkung zweiter Art). *Phys Z Sowjetunion* 8:457–471.
23. Kandasamy K, Lewis FA (1999) Important Gorsky effect influences on diffusion coefficients in metal-hydrogen systems. *Int J Hydrogen Energy* 24:763–769.
24. Mütschele T, Kirchheim R (1987) Segregation and diffusion of hydrogen in grain-boundaries of palladium. *Scr Metall* 21:135–140.
25. Weissmüller J, Lemier C (1999) Lattice constants of solid solution microstructures: The case of nanocrystalline Pd-H. *Phys Rev Lett* 82:213–216.
26. Pundt A (2004) Hydrogen in nano-sized metals. *Adv Eng Mater* 6:11–21.
27. Pundt A, Kirchheim R (2006) Hydrogen in metals: Microstructural aspects. *Ann Rev Mater Res* 36:555–608.
28. Lemier C, Weissmüller J (2007) Grain boundary segregation, stress and stretch: Effects on hydrogen absorption in nanocrystalline palladium. *Acta Mater* 55:1241–1254.
29. Shi S, Markmann J, Weissmüller J (2017) Actuation by hydrogen electrosorption in hierarchical nanoporous palladium. *Phil Mag* 97:1571–1587.
30. Porter DA, Easterling KE, Sherif M (2009) *Phase Transformations in Metals and Alloys* (CRC, Boca Raton, FL), 3rd Ed.
31. Brodowsky H, Poeschel E (1965) Wasserstoff in Palladium/Silber-Legierungen. *Z Phys Chem* 44:143–159.
32. Sakamoto Y, Ishimaru N, Mukai Y (1991) Thermodynamics of solution of hydrogen in Pd-Cu and Pd-Cu-Au solid solution alloys. *Berichte Bunsenges Phys Chem* 95:680–688.
33. Huang W, Opalka SM, Wang D, Flanagan TB (2007) Thermodynamic modelling of the Cu–Pd–H system. *Calphad* 31:315–329.
34. Flanagan TB, Wang Da, Luo S (2007) Thermodynamics of H in disordered Pd-Ag alloys from calorimetric and equilibrium pressure-composition-temperature measurements. *J Phys Chem B* 111:10723–10735.
35. Luo S, Wang D, Flanagan TB (2010) Thermodynamics of hydrogen in fcc Pd-Au alloys. *J Phys Chem B* 114:6117–6125.
36. Wicke E, Nernst GH (1964) Zustandsdiagramm und thermodynamisches Verhalten der Systeme Pd/H_2 und Pd/D_2 bei normalen Temperaturen; H/D-Trenneffekte. *Berichte Bunsenges Phys Chem* 68:224–235.
37. Flanagan TB, Oates WA (1991) The palladium-hydrogen system. *Ann Rev Mater Sci* 21:269–304.
38. Erlebacher J, Aziz MJ, Karma A, Dimitrov N, Sieradzki K (2001) Evolution of nanoporosity in dealloying. *Nature* 410:450–453.
39. McCue I, Benn E, Gaskey B, Erlebacher J (2016) Dealloying and dealloyed materials. *Annu Rev Mater Res* 46:263–286.
40. Mameka N, Markmann J, Jin H-J, Weissmüller J (2014) Electrical stiffness modulation–confirming the impact of surface excess elasticity on the mechanics of nanomaterials. *Acta Mater* 76:272–280.
41. Huber N, Viswanath RN, Mameka N, Markmann J, Weissmüller J (2014) Scaling laws of nanoporous metals under uniaxial compression. *Acta Mater* 67:252–265.
42. Lührs L, Zandersons B, Huber N, Weissmüller J (2017) Plastic Poisson's ratio of nanoporous metals: A macroscopic signature of tension–compression asymmetry at the nanoscale. *Nano Lett* 17:6258–6266.
43. Baranowski B, Majchrzak S, Flanagan TB (1971) The volume increase of fcc metals and alloys due to interstitial hydrogen over a wide range of hydrogen contents. *J Phys F* 1:258–261.
44. Peisl H (1978) Lattice strains due to hydrogen in metals. *Hydrogen in Metals I*, eds Alefeld G, Völkl J (Springer, Berlin), Vol 28, pp 69–70.
45. Mameka N, Wang K, Markmann J, Lilleodden ET, Weissmüller J (2016) Nanoporous gold—testing macro-scale samples to probe small-scale mechanical behavior. *Mater Res Lett* 4:27–36.
46. Brandes EA, Brook GB (2013) *Smithells Metals Reference Book* (Elsevier, Butterworth-Heinemann, Oxford).
47. Soyarslan C, Bargmann S, Pradas M, Weissmüller J (2018) 3D stochastic bicontinuous microstructures: Generation, topology and elasticity. *Acta Mater* 149:326–340.
48. Salama K, Ko CR (1980) Effect of hydrogen on the temperature dependence of the elastic constants of palladium single crystals. *J Appl Phys* 51:6202–6209.
49. Sandys-Wunsch M, Manchester FD (1992) Spinodal temperatures for macroscopic density fluctuations in Pd-H. II. elastic constants above the critical point. *J Phys Cond Matt* 4:2149–2154.
50. Schwarz RB, Bach HT, Harms U, Tuggle D (2005) Elastic properties of Pd–hydrogen, Pd–deuterium, and Pd–tritium single crystals. *Acta Mater* 53:569–580.
51. Safarik DJ, et al. (2010) Composition dependence of the elastic constants of β-phase and ($\alpha + \beta$)-phase PdH_x. *Ultrasonics* 50:155–160.
52. Hsu DK, Leisure RG (1979) Elastic constants of palladium and β-phase palladium hydride between 4 and 300 K. *Phys Rev B* 20:1339–1344.
53. Ho E, Goldberg HA, Weatherly GC, Manchester FD (1979) An in situ electron microscope study of precipitation in palladium-hydrogen alloys. *Acta Metall* 27:841–853.
54. Gleiter H, Weissmüller J, Wollersheim O, Würschum R (2001) Nanocrystalline materials: A way to solids with tunable electronic structures and properties?. *Acta Mater* 49:737–745.
55. Weissmüller J, Sieradzki K (2018) Dealloyed nanoporous materials with interface-controlled behavior. *MRS Bull* 43:14–19.